Assessing exchange-correlation functional performance in the chalcogenide lacunar spinels GaM_4Q_8 (M = Mo, V, Nb, Ta; Q = S,Se)

Yiqun Wang, Danilo Puggioni, and James M. Rondinelli [*]
Department of Materials Science and Engineering, Northwestern University, Evanston, Illinois 60208, USA

We perform systematic density functional theory (DFT) calculations to assess the performance of various exchange-correlation potentials V_{xc} in describing the chalcogenide GaM_4Q_8 lacunar spinels (M = Mo, V, Nb, Ta; Q = S, Se). We examine the dependency of crystal structure (in cubic and rhombohedral symmetries), electronic structure, magnetism, optical conductivity, and lattice dynamics in lacunar spinels at four different levels of V_{xc}: The local density approximation (LDA), generalized gradient approximation (GGA), meta-GGA, and hybrid with fractional Fock exchange. We find that LDA underperforms the Perdew-Burke-Ernzerhof (PBE) and PBE revised for solids (PBEsol) GGA functionals in predicting lattice constants as well as reasonable electronic structures. The performance of LDA and GGAs can be improved both quantitatively and qualitatively by including an on-site Coulomb interaction (LDA/GGA $+ U$) with a Hubbard U value ranging from 2 to 3 eV. We find that the PBE functional is able to produce a semiconducting state in the distorted polar $R3m$ phase without on-site Coulomb interactions. The meta-GGA functional SCAN (strongly constrained and appropriately normed) predicts reasonable lattice constants and electronic structures; it exhibits behavior similar to the GGA $+ U$ functionals for small U values of 1 to 2 eV. The hybrid functional HSE06 is accurate in predicting the lattice constants but leads to a band gap greater than the experimental estimation of 0.2 eV in this family. All of the lacunar spinels in the cubic phase are metallic at these levels of band theory; however, the predicted valence bandwidths are extremely narrow (≈ 0.5 eV). The DFT ground states of cubic vanadium chalcogenides are found to be highly spin polarized, which contrast with previous experimental results. With spin-orbit coupling (SOC) interactions and a Hubbard U value of 2 to 3 eV, we predict a semiconducting cubic phase in all compounds studied. SOC does not strongly impact the electronic structures of the symmetry-broken $R3m$ phase. We also find that these V_{xc} potentials do not quantitatively agree with the available experimental optical conductivity on GaV_4S_8; nonetheless, the LDA and GGA functionals correctly reproduce its lattice dynamical modes. Our findings suggest that accurate qualitative and quantitative simulations of the lacunar spinel family with DFT requires careful attention to the nuances of the exchange-correlation functional and considered spin structures.

I. INTRODUCTION

The lacunar spinel family GaM_4Q_8 (M = Mo, V, Nb, Ta; Q = S,Se) have garnered attention for decades owing to their fascinating properties, which include metal-insulator transitions [1], the capability to host skyrmion lattices [2], and multiferroism [3]. GaV_4S_8 and $GaMo_4S_8$ are the most well-studied materials in this family; they exhibit Jahn-Teller-type structural phase transitions at ≈ 40 K upon cooling, followed by spontaneous magnetic ordering below their Curie temperatures T_C [4]. The multiple phase transitions—metallic to insulating and paramagnetic to ferromagnetic—connecting distinct physical states make these transition-metal compounds ideal candidate materials for novel electronic platforms [5].

After decades of continuous studies on various properties of the lacunar spinel compounds, the mechanism of these phase transitions as well as the proper theoretical approaches to describe various electronic states are still unclear. For instance, while the vanadium and molybdenum compounds

can undergo symmetry-lowering structural phase transitions at low temperature [6–8], the niobium and tantalum lacunar spinels remain in the high-symmetry cubic phase over a broad temperature range [9]. One of the possible reasons for this behavior in the family may be attributed to variations in the strength of electron-electron interactions [6], since electron-correlation effects are expected to be stronger in $3d$ rather than $5d$ transition metals. However, there is also evidence that local structural distortions in lacunar spinel compounds could lead to insulating states even in the absence of strong correlation [10]. In addition, a number of members within the lacunar spinel family exhibit interesting resistive-switching behavior [11], making them potential materials for resistive random-access memory (RRAM) materials. Much of the literature attributes the aforementioned features to the special tetrahedral transition-metal clusters within the unit cell [12]; yet, how and why it supports all of these properties remains to be agreed upon [4,13,14]. In order to have a better understanding of the structure-property relationships among the lacunar spinels, a qualitative and possibly quantitative investigation of electron-correlation effects and structural distortions within these materials is needed.

[*]jrondinelli@northwestern.edu

Density functional theory (DFT) simulations are widely used in solid-state materials research owing to the efficiency and accuracy they achieve by replacing the original many-electron interaction problem with an auxiliary independent-particle problem through a suitably constructed exchange-correlation potential (V_{xc}). Because DFT simulations can capture the interplay of structural effects on electron-electron interactions and its dependence on determining the ground state, it is an ideal method to study the lacunar spinels with many internal atomic, spin, and orbital degrees of freedoms. However, no available V_{xc} can provide the exact description of exchange and correlation, which necessitates benchmarking both common and state-of-the-art density functionals against available experimental data. To that end, it becomes possible to identify the optimal functional for describing and predicting properties in the lacunar spinel family.

In this work, we systematically benchmark the performance of DFT V_{xc} functionals in describing the lacunar spinel family at four rungs of "Jacob's ladder," specifically the local density approximation (LDA), the generalized gradient approximation (GGA) as implemented by Perdew-Burke-Ernzerhof (PBE) and PBE revised for solids (PBEsol), the meta-GGA functional SCAN, and the hybrid functional HSE06. Our aim is to identify the best description of the lacunar spinel family from first-principles DFT simulations and where compromises on performance are made so as to to facilitate future studies and predictions. To that end, we investigate the functional dependency of lattice parameters, magnetism, electronic structures, optical properties, and lattice dynamics in both the cubic and Jahn-Teller distorted rhombohedral phases. Our main conclusion is that GGA and higher level V_{xc} functionals are more reasonable than LDA in predicting almost all properties assessed. The GGA functionals with an on-site Coulomb interaction (GGA + U) values of $U \approx 2$ eV quantitatively improves functional performance for the electronic structures of the rhombohedral phases. Spin-orbit coupling (SOC) interactions lift orbital degeneracies in the electronic structures of the cubic phases and enable a semiconducting phase to emerge with on-site Coulomb repulsion U values ranging from 2 to 3 eV. However, SOC does not significantly impact the electronic structures of the rhombohedral phase, where orbital symmetry is already broken by lattice distortions. SCAN and HSE06 are able to predict accurate lattice parameters, but HSE06 leads to band gaps significantly larger than experimental estimations. Our findings suggest that the predicted physical properties of the lacunar spinel family are highly V_{xc} functional dependent. Therefore, it is important to benchmark different V_{xc} performance on properties of interest before further studies. It is likely that the coupling of internal degrees of freedom in lacunar spinels, e.g., local cluster distortion, intra- and intercluster electronic and magnetic interactions, underlie the observed fascinating behavior as well as our reported high sensitivity to V_{xc} in this materials family.

II. MATERIALS AND METHODS

A. Crystal structure, electrical, and magnetic properties

The crystal structure of the lacunar spinel, also referred to as an A-site deficient spinel (AM_4Q_8), is derived from the reg-
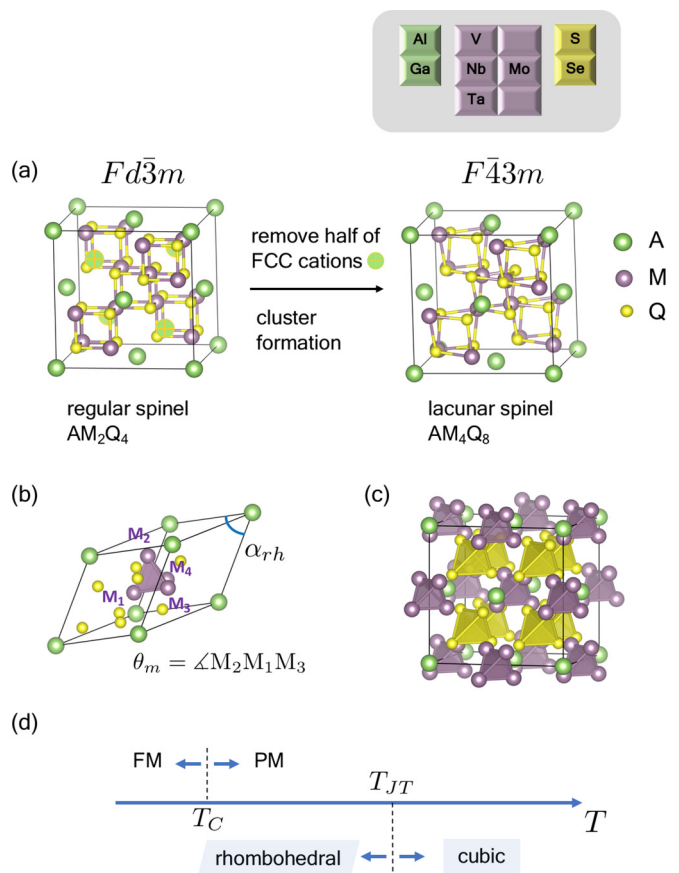

FIG. 1. (a) Derivation of the cubic phase lacunar spinel AM_4Q_8 from an ideal spinel structure; some anions are hidden in the figure to facilitate visualization of the M_4 cluster formation. (b) The primitive cell of AM_4Q_8 in both cubic and rhombohedral phases, with the interaxial rhombohedral angle α_{rh}, intracluster metal-metal-bond angle θ_m. (c) M_4 cluster connectivity in the cubic phase; they occupy the four octahedral holes created by the A cation vacancies. (d) Schematic phase diagram of lacunar spinels exhibiting multiple phase transitions. (Key: FM, ferromagnetic; PM, paramagnetic).

ular spinel (AM_2Q_4 composition) by removing the interpenetrating FCC A-site sublattice as depicted in Fig. 1(a). Upon removing half of the A-site cations occupying the tetrahedral holes in the regular spinel, the space group loses inversion symmetry, reducing from $Fd\bar{3}m$ (space group no. 227) to $F\bar{4}3m$ (space group no. 216). The structure then undergoes additional internal displacements and spontaneous strains: The previously equidistant M-M network breaks into isolated tetrahedral transition-metal clusters with chalcogenide ligands $[M_4Q_4]^{5+}$. In order to quantitatively describe the internal degrees of freedom in the crystal structure, we define α_{rh} as the interaxial angle of the rhombohedral unit cell, and θ_m as the M_2-M_1-M_3 angle centering the apical metal atom along the C_{3v} axis of the M_4 cluster, as shown in Fig. 1(b).

At room temperature, all lacunar spinels studied here exhibit cubic $F\bar{4}3m$ symmetry with $\alpha_{rh} = \theta_m = 60°$. GaV$_4S_8$, GaV$_4Se_8$, GaMo$_4S_8$, and GaMo$_4Se_8$, however, undergo symmetry-lowering structural Jahn-Teller (JT) transitions at ≈ 40 K from $F\bar{4}3m$ to $R3m$ (space group no. 160) [6–8], followed by spontaneous magnetic ordering at a lower Curie

TABLE I. Experimental Jahn-Teller (T_{JT}) and Curie (T_C) transition temperatures and unit cell volumes (V) for the distorted $R3m$ vanadium and molybdenum lacunar spinels. The vanadium (molybdenum) chalcogenides exhibit acute (obtuse) angluar distortions away from the ideal cubic $60°$. θ_m and α_{rh} are obtained at temperatures below T_{JT}, and no significant structural changes have been observed around T_C.

Compound	T_{JT} (K)	T_C (K)	α_{rh} (°)	θ_m (°)	$V_{cell}^{F\bar{4}3m}$ (Å^3)	V_{cell}^{R3m} (Å^3)	Ref.
GaV$_4$S$_8$	44	12.7	59.6	58.4	225.6	224.3	[3,15]
GaV$_4$Se$_8$	41	17.5	59.6	57.7	260.7	259.6	[16,17]
GaMo$_4$S$_8$	45	19.5	60.5	61.6	230.1	230.0	[7,15]
GaMo$_4$Se$_8$	45	23	60.6	61.4	263.3	262.2	[8]

temperature T_C [Fig. 1(d)]. These displacive distortions lead to a unit cell of slightly different volume, lattice parameters, and rhombohedral angle α_{rh}. The geometry of the metal cluster within the unit cell is also distorted away from its cubic structure and the θ_m angle deviates from the ideal cubic value ($60°$). The experimental crystallographic data for the distorted vanadium and molybdenum lacunar spinels are tabulated in Table I, where we also provide the Jahn-Teller and Curie transition temperatures.

The lacunar spinels are reported to be narrow-bandwidth semiconductors with ≈ 0.2 eV band gaps that vary with temperature [3–5]. Early work showed that the valence bands mainly consist of transition-metal d orbitals [18]. Since the transition-metal M_4 clusters are relatively distant from each other with about 4 Å intercluster separation [Fig. 1(c)], the low-energy valence electronic structure can be described using a molecular orbital (MO) diagram for the cluster (Fig. 2). In the cubic phase, the valance bands are triply degenerate with t_2 symmetry. V, Nb, and Ta chalcogenide lacunar spinels all exhibit t_2^1 occupancies whereas Mo exhibits t_2^5 filling, indicating susceptibility to a first-order Jahn-Teller distortion. After the Jahn-Teller structural distortion, the triply degenerate t_2 orbital splits into two sets of orbitals, a_1 and e. The relative energy of the two sets of orbitals is occupancy

dependent; the a_1 orbital is more stable in the vanadium compounds, whereas the e orbitals are preferentially stabilized in the molybdenum compounds.

In addition to these structural transitions, the vanadium and molybdenum compounds show spontaneous magnetic ordering at T_C when in the rhombohedral phase. GaV$_4$S$_8$ is also reported to have a complex magnetic phase diagram at low temperature [2]. The effective local magnetic moment in both the paramagnetic and ferromagnetic phases corresponds to approximately one unpaired electron per unit cell and is mostly localized about the transition-metal cluster [4] rather than on the individual atomic sites constituting the cluster. GaNb$_4$S$_8$, GaNb$_4$Se$_8$, and GaTa$_4$Se$_8$ are paramagnetic at ambient conditions with effective magnetic moments of 1.8, 1.6, and 0.7 μ_B per cluster [9,19]. No structural phase transitions or spontaneous magnetic orderings are reported in these compounds down to 1.6 K [9]. Last, we note that the family of materials is also often referred to as Mott insulators owing to the large distance between transition-metal clusters [4] and not typically because of strong electron-electron interactions [10], although they likely play some role. The semiconducting behavior is typically attributed to variable range hopping (VRH) conduction [6] among these separated metal clusters. Nonetheless, the microscopic mechanisms behind the semiconducting nature, as well as the multiple phase transitions, are still under active investigation [3,20].
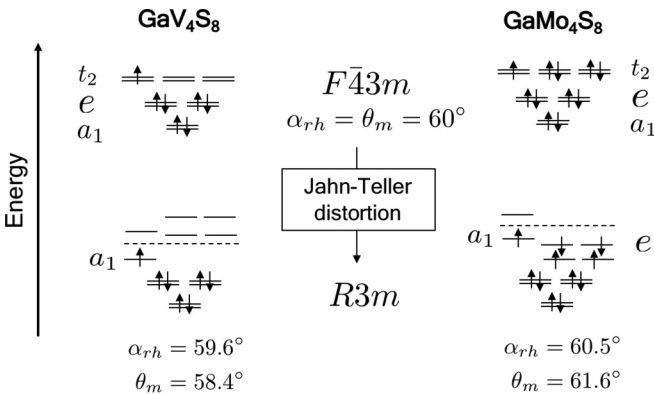
B. Exchange-correlation functionals

We use exchange-correlation potentials (V_{xc}) at four different levels of approximation to assess the structure and properties of the chalcognide lacunar spinels. The functionals examined include LDA, GGA as implemented by Perdew-Burke-Ernzerhof (PBE) [21], and PBE revised for solids (PBEsol) [22], meta-GGA functional SCAN as implemented by Sun *et al.* [23], and Heyd-Scuseria-Ernzerhof hybrid functional HSE06 [24]. The V_{xc} in LDA is not derived from first principles, but from Monte Carlo simulations of the uniform electron gas. The functional solely depends upon the local electron density in space and usually provides a good approximation for simple materials (including metals) with electronic states that vary slowly in space. However, the LDA potential decays rapidly for finite systems while the true exchange-correlation potential has significant nonlocal contributions; this behavior often leads to overestimation of the binding energy [25] and underestimation of lattice constants in solids [26].

FIG. 2. Valence molecular orbital diagrams of GaV$_4$S$_8$ and GaMo$_4$S$_8$. The valence t_2-symmetry orbitals are triply degenerate in the cubic phase. The orbital degeneracy is lifted by the accompanied Jahn-Teller distortion with a distortion sense that stabilizes and leads to filling of either the a_1 (GaV$_4$S$_8$) or e (GaMo$_4$S$_8$) orbitals based on orbital occupancy of the metals forming the cluster. The dotted lines indicate the Fermi level in the distorted phases, whereas in the cubic phase the Fermi level intersects the triply degenerate valence bands.

To improve on the LDA, GGA functionals that take the gradient of the electron density $\nabla n(\mathbf{r})$ into consideration have been developed. The PBE and PBEsol functionals improve the binding energy by roughly an order of magnitude, but have a general tendency to overestimate lattice constants [26]. Since LDA and GGA functionals are well known to be unable to predict the insulating state of Mott insulators [27] with strong correlations and nonlocal exchange, the beyond-DFT method, DFT + U, is typically used to account for such interactions among the localized d electrons. The on-site Coulomb interaction term U favors the on-site occupancy matrix toward fillings that are fully occupied or fully unoccupied and hence a more localized electronic structure within the correlated manifold. Here, we use the GGA functionals PBE and PBEsol with on-site Coulomb interaction (GGA + U) with U values of 1.0, 2.0, and 3.0 eV on the M-metal sites using the formalism introduced by Dudarev *et al.* [28] to assess the effect of electron correlation in the M_4 clusters. The range of U values is based on results from previous computational studies[19,29,30] and our own preliminary assessments, where we focused on reasonable band gap and magnetic moment predictions.

It comes naturally from the previous two rungs of Jacob's ladder that the second-order derivative of the electron density should be considered. Meta-GGA functionals are essentially an extension to GGAs whereby the Laplacian of the electron density $\nabla^2 n(\mathbf{r})$ is also considered. In practice, the kinetic energy density $\tau(\mathbf{r}) = \sum_{i=1}^{N_{occ}} \frac{1}{2}|\nabla \psi_i(\mathbf{r})|^2$ is used, where the summation runs over the occupied Kohn-Sham orbitals $\psi_i(\mathbf{r})$. The recently developed meta-GGA functional SCAN fulfills all known constraints required by the exact density functional and is reported to achieve remarkable accuracy for systems where the exact exchange-correlation hole is localized around its electron [23].

Hybrid DFT functionals incorporate a portion of exact exchange interaction from Hartree-Fock (HF) theory with that of a local or semilocal density functional. The semiempirical hybrid functional B3LYP is widely used for finite chemical systems and gives more accurate thermochemical and electronic properties [31,32]. In periodic solid-state systems, one route to incorporate an exact exchange interaction is by means of range separation. In the range-separated HSE06 hybrid functional, the short-range (SR) exchange interaction consists of partial contributions from exact exchange and the PBE functional. The long-range (LR) part of the Fock exchange term is replaced by that from the semilocal PBE functional. The correlation term from PBE is used in the HSE06 hybrid functional. The resulting exchange-correlation energy expression is

$$E_{xc}^{\text{HSE06}} = \frac{1}{4}E_x^{\text{HF,SR}} + \frac{3}{4}E_x^{\text{PBE,SR}} + E_x^{\text{PBE,LR}} + E_c^{\text{PBE}}.$$

The inclusion of exact-exchange interactions in hybrid functionals also partly fixes the self-interaction problem in pure DFT functionals and can provide accurate descriptions of lattice parameters, bulk moduli, and band gaps in periodic systems [33–35].

C. Computational details

We perform DFT simulations as implemented in the Vienna *Ab initio* Simulation Package (VASP) [36,37]. The projector augmented-wave (PAW) potentials [38] are used for all elements in our calculations with the following valence electron configurations: Ga ($3d^{10}4s^24p^1$), Mo ($4s^24p^64d^55s^1$), V ($3s^23p^63d^44s^1$), Nb ($4s^24p^64d^45s^1$), Ta ($5p^65d^46s^1$), S ($3s^23p^4$), and Se ($4s^24p^4$). Based on convergence test with respect to k-point meshes in reciprocal space and plane-wave basis set cutoff energies, we use a Γ-centered $6 \times 6 \times 6$ mesh with a 500-eV kinetic energy cutoff. For HSE06 calculations, we use a $4 \times 4 \times 4$ k-point mesh and a 400-eV kinetic energy cutoff due to the high computational cost and convergence difficulties for the spin-polarized calculations. Since the lacunar spinels are small-gap semiconductors, we employ Gaussian smearing with a small 0.05 eV width. For density-of-state (DOS) calculations, we use the tetrahedron method with Blöchl corrections [39].

We perform full lattice relaxations with different DFT functionals until the residual forces on an individual atom are less than 1.0 meV Å^{-1}. The experimental crystal structures of the lacunar spinels GaV$_4$S$_8$, GaV$_4$Se$_8$, GaMo$_4$S$_8$, GaMo$_4$Se$_8$, GaNb$_4$S$_8$, GaNb$_4$Se$_8$, and GaTa$_4$Se$_8$ are obtained from the Inorganic Crystal Structure Database (ICSD) [40] and used as initial inputs for these geometry relaxations. GaTa$_4$S$_8$ is not included here since the structure is not experimentally reported. Both high-temperature cubic and low-temperature rhombohedral phases are investigated for all target compounds. Crystal structures of the rhombohedral phase Nb and Ta compounds are obtained by making a small displacement to their cubic atomic positions along the symmetry-lowering pathway (i.e., from $F\bar{4}3m$ to $R3m$), followed by DFT structural relaxations. All experimental and DFT-relaxed crystal structures are available electronically at Ref. [41].

The effect of on-site Coulomb interactions on the crystal structures is also investigated at the LDA and GGA functional level. Since the lacunar spinels exhibit various magnetic properties, we also initialize the calculations with multiple possible magnetic configurations for the lattice relaxations. This is a necessary process owing to the multiple metastable spin configurations accessible. The magnetic configuration with the lowest energy is reported as the DFT ground state and used to compare with other functional results. Spin-orbit interactions are also considered in our electronic structure simulations owing to their potentially significant impact on the orbital structure of $4d$ and $5d$ transition metals. For spin-orbit coupling (SOC) calculations, we use the fully relaxed crystal structures from the aforementioned non-SOC simulations. The magnetization is set to be $1\mu_B$ per formula unit uniformly distributed on four transition metal sites along the (111) direction for both the cubic and rhombohedral phases.

Zone center ($\mathbf{k} = \mathbf{0}$) phonon frequencies and eigendisplacements for both the cubic and rhombohedral phases of GaV$_4$S$_8$ (within primitive cells) are obtained using the frozen-phonon method with pre- and postprocessing performed with the PHONOPY package [42].
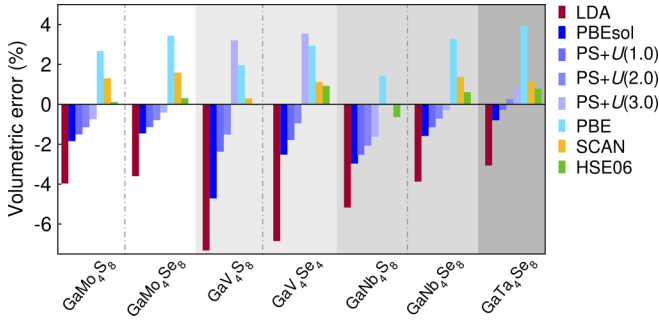
FIG. 3. Relative error in the unit cell volume of the cubic phase at different levels of DFT. PS is an abbreviation for the PBEsol functional and the number in parentheses is the value of the on-site Coulomb interaction used in the GGA + U method.

III. RESULTS AND DISCUSSION

A. $F\bar{4}3m$ cubic phase

1. Lattice parameters

The crystal structures of the lacunar spinels with cubic symmetry are fully relaxed with DFT using the different V_{xc} potentials. Figure 3 shows the volumetric error for the DFT ground-state unit cell volume relative to the experimental room temperature data. For molybdenum and vanadium compounds, we report the cell volumes of ferromagnetic spin structures with magnetizations of 1 and 5 μ_B per formula unit, respectively. The niobium and tantalum compounds are nonmagnetic with all DFT functionals. See Sec. III A 2 for the detailed descriptions of the magnetic moment configurations.

In general, the LDA and PBEsol functionals underestimate the lattice parameters, while PBE predicts larger lattice constants compared with experimental data. LDA has relatively larger deviations (4% or higher) compared with the GGA results; it is a well-known problem that LDA tends to underestimate the lattice constants. We also check the effect of on-site Coulomb interactions (LDA and GGA + U) on lattice parameters with U values up to 3 eV. With increasing on-site Coulomb interaction strength, we find the lattice parameters follow a monotonic increasing trend for both the LDA and GGA functionals. We only show the trend for PBEsol in Fig. 3 owing to its similarity with the others. Therefore, a reasonable Hubbard U value could quantitatively improve the lattice parameter predictions in the LDA and PBEsol functionals.

Interestingly, the vanadium compounds exhibit cell volumes that are the most sensitive to the choice of the U value among the lacunar spinels. For instance, the difference in volumetric error induced by $U = 3.0$ eV is less than 2% in GaMo$_4$S$_8$, but is almost 8% in GaV$_4$S$_8$. The highly spin-polarized electronic state used for the vanadium compounds may be a possible cause of the different sensitivity on the on-site Coulomb interactions.

GGA functionals with $U < 3.0$ eV generally predict reasonable cubic lattice constants with less than 4% error in the cell volumes. The meta-GGA functional SCAN and hybrid functional HSE06 have smaller errors in predicting lattice constants, which give less than 2% error for all seven compounds studied here. Considering the high computational cost of structural relaxations with HSE06, SCAN should be preferred over HSE06 for lattice parameter estimation unless one requires a specific accuracy requirement or improved forces.

These results suggest that most of the DFT functionals are able to predict reasonable cubic phase crystal structures in the lacunar spinel family with less than 4% error in the volumes. Generally, we recommend using GGA functionals with a tunable on-site Coulomb repulsion U value of 1 to 3 eV for lattice parameter predictions. SCAN and HSE06 give more accurate lattice constants compared with lower-level functionals, while SCAN is preferable based on a compromise between accuracy and efficiency.

2. Magnetism

Experimentally, the vanadium and molybdenum compounds exhibit paramagnetism above their Curie temperatures and exhibit spontaneous magnetic ordering at low temperature [4]. The magnetically ordered phases can host multiple fascinating magnetic states, including ferromagnetism and complex spin textures (skyrmion lattices) [2]. Those complex magnetic structures are not considered here. The niobium and tantalum compounds show very weak magnetism and do not exhibit spontaneous magnetic ordering down to 1.6 K [9]. Since the transition-metal clusters are relatively far from each other with a distance of around 4 Å, the intercluster magnetic interactions are expected to be quite small. Here, we use a ferromagnetic spin configuration on all metal sites within the cluster to model the magnetically ordered phases.

From our DFT simulations, different transition-metal clusters are able to host various magnetic configurations. For the molybdenum compounds, we are only able to stabilize one ferromagnetic configuration in the cubic phase which corresponds to 1 μ_B per primitive cell. The magnetic moments are evenly distributed about the four molybdenum atoms in the Mo$_4$ cluster with negligible contributions from other atomic species. In contrast, the vanadium compounds show numerous stable magnetic configurations (Table II). Apart from the same ferromagnetic configuration as in the molybdenum compounds, we also find a highly spin-polarized state in the cubic phase. To the best of our knowledge, the electronic structures of this state has not yet been reported before. Recent neutron diffraction studies show that there is one single spin distributed across the V$_4$ cluster instead of it residing on a single vanadium ion [43].

In the highly spin-polarized state, the magnetization could be 5 or 7 μ_B per formula unit (f.u.), depending on the DFT functional used. The spin moments are evenly distributed about the transition-metal cluster, with approximately 1.25 μ_B magnetic moment localized on each vanadium atom. This state is significantly lower in energy than the ferromagnetic configuration with 1 μ_B/f.u. per formula unit in our DFT simulations.

In several cases, we are not able to stabilize some of the magnetic configurations for vanadium compounds (indicated by empty cells in Table II). For example, LDA only converges to nonmagnetic configurations, and PBE + $U = 2.0$ eV cannot stabilize the state with 1 μ_B per cluster. In cases where both states can be stabilized, however, the more strongly spin-polarized state is always significantly more stable than the
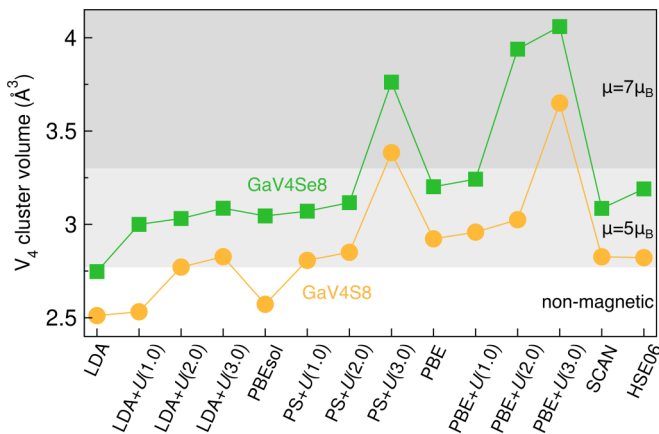
FIG. 4. The volume of the tetrahedral V_4 cluster with different DFT functionals and their corresponding ground-state magnetic moment per formula unit. The white area shows nonmagnetic results. The light-shaded and dark-shaded areas correspond to states with 5 and 7 μ_B magnetic moments, respectively. PS is an abbreviation for the PBEsol functional and the number in parentheses is the value of the on-site Coulomb interaction used in the GGA $+ U$ method.

other two configurations (Table II). We also observe a trend that the highly polarized state is more favored with larger on-site Coulomb interactions or with higher level DFT functionals. In addition, the $\mu = 1$ μ_B state is usually energetically closer to the nonmagnetic state than the highly spin-polarized state. These ground-state magnetic configurations are also sensitive to the V_4 cluster volume, which we show varies with different levels of DFT functional (Fig. 4). A larger V_4 cluster usually supports a higher magnetic moment, while a smaller volume leads to reduced or quenched moments. Our findings show that local structure and magnetic moments are correlated with each other and should be assessed carefully

TABLE II. Energy differences (in eV/f.u.) of different magnetic configurations compared with nonmagnetic calculations for the cubic phase. E_σ denotes the energy of the highly polarized state with 5 or 7 μ_B per formula unit. An empty cell indicates that the state was not stable. PS is an abbreviation for the PBEsol functional and the number in parentheses is the value of the on-site Coulomb interaction used in the GGA $+ U$ method.

	GaV_4S_8		GaV_4Se_8	
	E_σ	$E_{\mu=1\mu_B}$	E_σ	$E_{\mu=1\mu_B}$
LDA				
LDA $+ U$(1.0)		0.005	−0.172	−0.007
LDA $+ U$(2.0)	−0.404	−0.008	−0.68	0.06
LDA $+ U$(3.0)	−0.946	−0.03	−1.264	−0.051
PBEsol		−0.001	−0.072	−0.008
PS $+ U$(1.0)	−0.305	−0.014	−0.562	−0.028
PS $+ U$(2.0)	−0.823	−0.035	−1.123	
PS $+ U$(3.0)	−1.641		−2.174	
PBE	−0.095	−0.010	−0.327	−0.022
SCAN	−0.875	−0.049	−1.196	−0.064
HSE06	−1.355	0.005	−1.742	−0.092

because both depend on the choice of exchange-correlation functional. A recent study utilizing dynamical mean-field theory simulations showed similar results, where the significance of electron correlations in describing the MO Mott physics and structural properties of GaV_4S_8 is also reported [44].

There is also evidence that local cluster distortions still exist above the Jahn-Teller temperature [45] and that the symmetry-broken V_4 cluster could lead to different magnetic configurations that are in better agreement with experimental results [29]. This occurs because of the physics of the distorted phase described in Sec. III B. To that end, we suggest high-resolution detection methods (e.g., pair distribution function) be used to probe the local structures of cubic phase lacunar spinels.

Last, the niobium and tantalum compounds are always nonmagnetic in our calculations, regardless of the initial magnetic configuration or choice of DFT functional. This may be a consequence of strong but geometrically frustrated antiferromagnetic interactions in the cubic Nb and Ta clusters [19] or due to a reduction in the on-site Hund's interactions, which drives moment formation, from the greater hybridization due to the extended $4d$ and $5d$ orbitals.

3. Electronic structures

We next use the relaxed cubic crystal structure and ground-state magnetic configuration of each compound and examine the electronic structures (Fig. 5). According to the idealized charge distribution in $Ga^{3+}[M_4Q_4]^{5+}Q_4^{2-}$, the number of electrons per V_4, Nb_4, and Ta_4 cluster is 7 (since they are in the same column of the periodic table) while there are 11 electrons for a Mo_4 cluster; these electrons fill the cluster orbitals depicted in Fig. 2.

We selectively show the electronic structures of GaV_4S_8, $GaMo_4S_8$, $GaNb_4Se_8$, and $GaTa_4Se_8$ in Fig. 5 because their S/Se counterpart compounds with the same transition-metal cluster exhibit similar band properties. From our PBE-DFT band structures and projected DOSs for the molybdenum, niobium, and tantalum compounds (Fig. 5(a)[1,3,4]), we find six valence bands mainly consisting of transition-metal d-orbital character with relatively small contribution from the anion p orbitals. The triply degenerate band (t_2 MO symmetry) is higher in energy than the doubly (e MO) and singly (a_1 MO) degenerate bands. The band degeneracy and ordering agree well with the cluster MO descriptions of the low-energy electronic structure in these compounds.

The DFT ground-state electronic structures of the cubic phase vanadium compounds, however, are significantly different from the other chalcogenides in the lacunar spinel family (Fig. 5(a)[2]). All six valence bands in the spin-up channel (green bands) are fully occupied, while only the lower part of the spin-down channel is partially occupied. The triply degenerate spin-down bands are shifted ≈ 1 eV above the Fermi level. Interestingly, the metastable magnetic state with 1 μ_B per cluster exhibits band dispersions that are more similar to the rest of the family (Fig. 6) and the magnetic moment of 1 μ_B agrees better with experimental results. It remains unknown whether this DFT ground state in the cubic phase is stable and experimentally accessible; further low-temperature
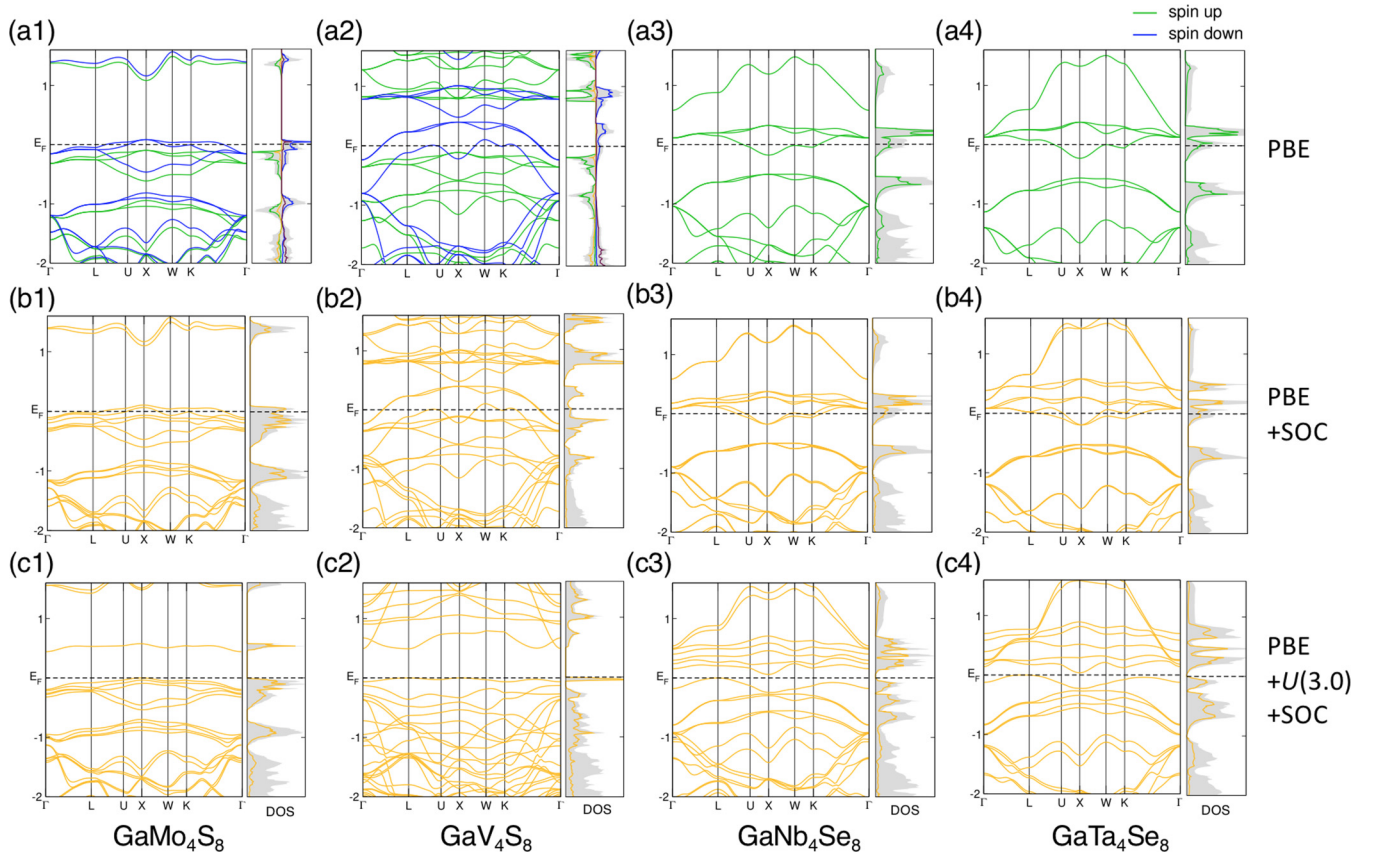
FIG. 5. DFT-PBE ground-state band structures and projected density of states (DOS) of the cubic lacunar spinels within a primitive cell. The Fermi level (E_F) is indicated by a broken line; the vertical energy axis is in units of eV. The gray shaded areas in the DOS panels correspond to the total electronic density of states. The second and third rows show results with SOC included, as indicated in the rightmost column. The orange curve in the DOSs represent the contribution from the transition metal cluster.

neutron-based scattering measurements, for example, could be used to probe the existence of this spin configuration.
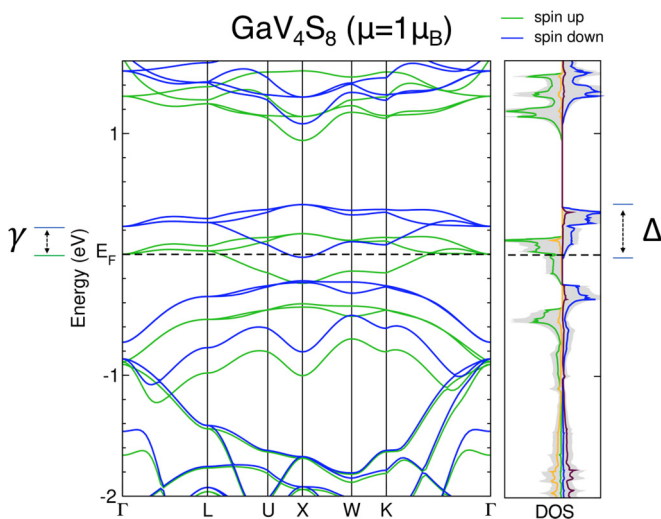

FIG. 6. DFT-PBE band structure and DOS of metastable cubic GaV$_4$S$_8$ with 1 μ_B per formula unit. We define γ as the exchange splitting between different spin channels and Δ as the splitting of the three valence bands at the X point. Here, those bands are located approximately at E_F and $E_F + 0.3$ eV.

We next quantitatively assess the impact of different V_{xc} as well as on-site Coulomb interactions on the electronic structures by defining two parameters, γ and Δ, as shown in Fig. 6, which describe the key features in the band structure. γ corresponds to the energy difference between different spin channels of the triply degenerate valence band at the Γ point. Δ quantifies the magnitude of the splitting among the triply degenerate minority-spin bands at the X point, $k = (1/2, 0, 1/2)$, near E_F. The values of γ and Δ for the chalcogenide lacunar spinels at different levels of DFT theory are tabulated in Table III. For the nonmagnetic Nb and Ta compounds, we only report Δ.

All of the cubic phase lacunar spinels are metallic from band theory without considering spin-orbit interactions. Figure 5 shows that the Fermi level, E_F, is always located within the valence bands, regardless of the magnetic configuration or DFT functional. Specifically, the cubic phase V and Mo compounds are predicted to be half-metals as only one spin channel crosses the Fermi level whereas the other spin-channel is fully gapped. In either group VB or VIB transition-metal compounds, there is an odd number of electrons in three degenerate bands (Fig. 2). For the low spin-polarized states with 1 μ_B/f.u., we then find that the Fermi level crosses this set of triply degenerate bands and metallicity is protected by the $F\bar{4}3m$ crystal symmetry. Here, the splitting of these triply degenerate valence bands throughout the

TABLE III. Electronic band splitting of the triply degenerate bands in the cubic lacunar spinels at different levels of DFT. γ quantifies the splitting between the two spin channels. Δ is the value of the band splitting among the triply degenerate bands at the X point in momentum space near E_F. For the vanadium compounds, these values are tabulated for different spin-magnetic moment states separately. An empty cell indicates that the state was not stable.

Compound		LDA	PBEsol	PBE	PBE + U(1.0)	PBE + U(2.0)	SCAN	HSE06
GaMo$_4$S$_8$	γ	0.09	0.15	0.16	0.22	0.28	0.22	0.56
	Δ	0.69	0.65	0.55	0.55	0.55	0.59	0.67
GaMo$_4$Se$_8$	γ	0.11	0.14	0.16	0.22	0.29	0.22	0.52
	Δ	0.50	0.48	0.38	0.39	0.40	0.44	0.52
GaV$_4$S$_8$	γ			1.13	1.58	2.01	1.76	3.1
(5 μ_B)	Δ			0.48	0.44	0.33	0.43	0.46
GaV$_4$S$_8$	γ		0.12	0.23	0.32		0.37	0.95
(1 μ_B)	Δ		0.52	0.41	0.40		0.43	0.55
GaV$_4$Se$_8$	γ		1.07	1.17	1.65	2.60	1.82	3.2
(5 μ_B)	Δ		0.42	0.36	0.34	0.20	0.35	0.51
GaV$_4$Se$_8$	γ		0.20	0.23	0.34		0.40	0.81
(1 μ_B)	Δ		0.37	0.30	0.28		0.31	0.41
GaNb$_4$S$_8$	Δ	0.88	0.82	0.69	0.71	0.71	0.73	0.86
GaNb$_4$Se$_8$	Δ	0.63	0.59	0.50	0.52	0.53	0.55	0.66
GaTa$_4$Se$_8$	Δ	0.74	0.71	0.60	0.63	0.63	0.65	0.69

Brillouin zone is quite small; although the Δ value is functional dependent, it does not exceed 0.7 eV. There is also a small trend of increasing splitting between different spin channels (γ) with higher level DFT functionals. We attribute this to the more accurate exchange interactions captured with the more advanced functionals.

The flat valence bands derived from these cluster orbitals lead to large effective masses, and these electrons should be highly localized in real space. This is in agreement with the fact that the transition-metal clusters are far from each other within the unit cell, and the electrons are localized within the cluster. One of the possible conduction mechanisms for the lacunar spinels is through variable-range hopping (VRH) [6]. It is for the same reason that these compounds have been called "Mott insulators" [4].

For the highly polarized magnetic state in the vanadium compounds, γ is much larger than Δ, which makes it different from the rest of the family. In this case, the Δ term may not be that important since the triply degenerate band is no longer the highest occupied band. The two bands crossing the Fermi level are the a_1 and e orbitals in the spin-down channel. It is therefore possible to obtain a semiconducting state by shifting the e-symmetry orbitals to higher energy and fully occupying the a_1 orbital. Indeed, we find such a state in GaV$_4$Se$_8$ using the SCAN functional, where the band gap is approximately 60 meV. Whether this highly polarized state is experimentally accessible, however, remains unclear.

We next report results with SOC included in our simulations. The band structures and DOSs with the PBE functional are shown in Fig. 5(b)[1–4]. Orbital degeneracy is partly broken compared with the non-SOC band structures. The broken symmetry here is vital for reproducing a semiconducting state since it enables further orbital splitting by increasing electron-electron interactions. Figure 5(c)[1–4] show the electronic structures with PBE + SOC and a U value of 3.0 eV, where all four compounds exhibit a small but finite band gap. It is interesting to note that both SOC and on-site Coulomb interactions are necessary to produce a semiconducting cubic

phase for all compounds studied. Intuitively, SOC serves the purpose of symmetry breaking in the highly symmetric cubic phase while on-site Coulomb interactions localize electrons and increase repulsion between bands, which eventually lead to a semiconducting state in the cubic lacunar spinels. Although the electron-correlation effect (modeled by the on-site Coulomb repulsion U) is typically considered more important in 3d transition metals, spin-orbit interactions are more significant in 5d transition metals. Indeed, the lacunar spinel compounds investigated, which include transition metals from the 3d, 4d, and 5d rows, exhibit similar yet nonidentical behaviors. This behavior could be the outcome of competing SOC and on-site Coulomb interactions within these transition-metal cluster systems. It also has been shown that spin-orbit coupling effects within the lacunar spinel system could lead to exciting physics (e.g., spin-orbital entangled molecular j_{eff} states) [46,47].

Our findings in the cubic phase lacunar spinels indicate that different DFT functionals, as well as various electron-electron and spin-orbital interactions, can lead to qualitatively different interpretations of their electronic and magnetic properties. Therefore, extra care in the exchange-correlational functional selection should be taken before pursuing extensive DFT simulations on this family.

B. *R3m* distorted phase

1. Lattice parameters

In this section, we investigate the DFT functional dependency of properties in the distorted rhombohedral phase. Since only molybdenum and vanadium compounds are reported to exhibit Jahn-Teller-type structural distortions, we benchmark the V_{xc} performance in predicting lattice parameters against available experimental data of GaV$_4$S$_8$, GaV$_4$Se$_8$, GaMo$_4$S$_8$, and GaMo$_4$Se$_8$. In all cases, we use a ferromagnetic spin configuration with 1μ_B magnetic moment per unit cell in our structural relaxations; see Sec. III B 3 for a detailed discussion of the magnetic moment configurations.
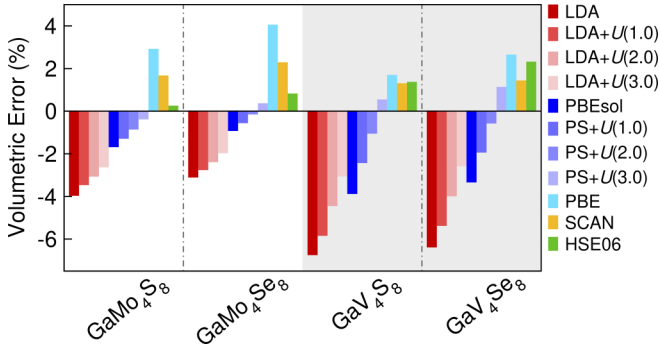
FIG. 7. Relative error of the rhombohedral unit cell volume at different levels of DFT. PS is an abbreviation for the PBEsol functional and the number in parentheses is the value of the on-site Coulomb interaction used in the LDA/GGA $+ U$ method.

The Jahn-Teller structural phase transition reduces the crystal symmetry from space group $F\bar{4}3m$ to $R3m$ and it occurs with a change in unit cell volume. The relative error of the fully relaxed unit cell volumes for the molybdenum and vanadium compounds are shown in Fig. 7. Here, we observe a similar trend as found in the cubic phase. The LDA and PBEsol functionals underestimate the ground-state lattice volume, while LDA shows larger deviations from the experimental data. Moreover, structural relaxations of the rhombohedral phases of GaV_4S_8 and $GaMo_4S_8$ with LDA converge to nonmagnetic cubic structures, regardless of the initial magnetic moment configurations. LDA is able to stabilize a ferromagnetic configuration in the rhombohedral phase only with on-site Coulomb interactions (LDA $+ U$).

PBE overestimates the lattice constants of all four compounds. With increasing value of the on-site Coulomb interactions, the lattice parameters also increase slightly. In the rhombohedral phase, the cell volume of the vanadium compounds is not as sensitive to the Hubbard-U value as in the cubic phase, presumably because the electronic structure is semiconducting in the $R3m$ symmetry. The SCAN and HSE06 functionals again perform quite well with regards to the lattice parameters with less than 2% error.

2. Internal degrees of freedom

The occupied Wyckoff sites of the transition metals also split upon the transition into the rhombohedral phase, leading to one apical site [M_1 in Fig. 1(b)] along the C_{3v} distortion axis and three basal atoms [M_2, M_3, M_4 in Fig. 1(b)] forming a plane perpendicular to the C_{3v} axis. The Wyckoff positions of the transition metals in $GaMo_4S_8$ and GaV_4S_8 with $R3m$ symmetry (space group no. 160) after structural relaxation with different exchange-correlation functionals are tabulated in Table IV. The selenide compounds show similar functional dependencies and are not shown here. In general, the changes in Wyckoff positions with respect to functional are quite small. However, we find that the z_1 value in GaV_4S_8 has a significantly higher functional dependency over that in $GaMo_4S_8$ (Fig. 8). Both increasing the value U as well as going to higher levels of exchange-correlation functionals favor larger structural distortions in GaV_4S_8, i.e., keeping the apical V atom far away from the center of the tetrahedral transition-

TABLE IV. Wyckoff positions of the transition metals in rhombohedral $GaMo_4S_8$ and GaV_4S_8 after structural relaxation with different DFT functionals. The z value of the $3a$ and $9b$ sites in space group no. 160 are labeled z_1, z_2, respectively. PS is an abbreviation for the PBEsol functional and the number in parentheses is the value of the on-site Coulomb interaction used in the GGA $+ U$ method.

	$3a$ (z_1)	$9b$ (x)	$9b$ (z_2)
	$GaMo_4S_8$		
Experimental [15]	0.4014	0.1956	0.2023
LDA	0.3982	0.1960	0.2022
PBEsol	0.4012	0.1951	0.2012
PS $+ U$(1.0)	0.4014	0.1950	0.2011
PS $+ U$(2.0)	0.4015	0.1949	0.2010
PS $+ U$(3.0)	0.4016	0.1948	0.2010
PBE	0.4020	0.1956	0.2009
SCAN	0.4029	0.1962	0.2006
HSE06	0.4025	0.1959	0.2007
	GaV_4S_8		
Experimental[15]	0.3910	0.1937	0.2013
LDA	0.3944	0.1946	0.1998
PBEsol	0.3913	0.1969	0.2005
PS $+ U$(1.0)	0.3877	0.1966	0.2005
PS $+ U$(2.0)	0.3856	0.1958	0.2005
PS $+ U$(3.0)	0.3834	0.1951	0.2008
PBE	0.3888	0.1972	0.2005
SCAN	0.3852	0.1963	0.2004
HSE06	0.3839	0.1956	0.2005

metal cluster. The z_1 Wyckoff position of the Mo atoms is also largely insensitive to the choice of the DFT functional, possibly owing to the reversed distortion in $GaMo_4S_8$, where steric effects might prohibit further distortion.

After the structural phase transition, both the rhombohedral angle α_{rh} and bond angle θ_m in the transition-metal cluster diverge from the cubic 60°, leading to a greater number of
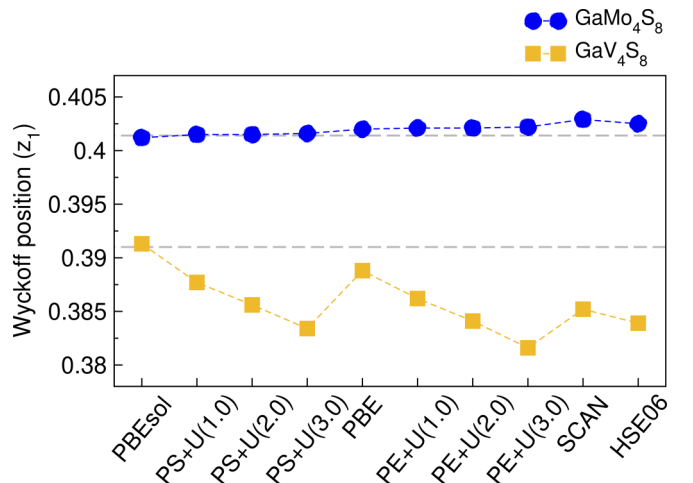

FIG. 8. The $3a$ (z_1) Wyckoff position in rhombohedral $GaMo_4S_8$ and GaV_4S_8 at different V_{xc}. The gray dashed lines correspond to the experimental values. PS is an abbreviation for the PBEsol functional and the number in parentheses is the value of the on-site Coulomb interaction used in the GGA $+ U$ method.

TABLE V. The unit cell rhombohedral angle α_{rh} (in deg) for the $R3m$ phases and the corresponding apical bond angle θ_m (in deg) for the transition-metal cluster at different levels of DFT functional. PS is an abbreviation for the PBEsol functional and the number in parentheses is the value of the on-site Coulomb interaction used in the GGA + U method.

	$GaMo_4S_8$		$GaMo_4Se_8$		GaV_4S_8		GaV_4Se_8	
	α_{rh}	θ_m	α_{rh}	θ_m	α_{rh}	θ_m	α_{rh}	θ_m
Experimental	60.47	61.60	60.57	61.43	59.62	58.38	59.56	57.72
LDA	60.00	60.00	60.78	62.76	60.00	60.00	59.55	57.71
PBEsol	60.70	62.29	60.80	62.91	59.56	57.67	59.33	56.59
PS + U(1.0)	60.75	62.50	60.81	63.00	59.28	56.39	59.20	56.00
PS + U(2.0)	60.76	62.59	60.81	63.06	59.16	55.91	59.09	55.60
PS + U(3.0)	60.77	62.66	60.81	63.12	58.99	55.26	58.87	54.75
PBE	60.73	62.53	60.79	63.07	59.36	56.62	59.26	56.09
SCAN	60.76	62.80	60.84	63.27	59.21	55.72	59.12	55.47
HSE06	60.77	62.74	60.79	63.15	59.05	55.38	58.94	55.04

internal degrees of freedom in the distorted phase. The latter is correlated with the change in occupied Wyckoff sites of the transition metals. We record these internal bond angles of the four lacunar spinels after structural relaxation using different DFT functionals; the results are shown in Table V.

Almost all DFT functionals (except for LDA) predict similar results for α_{rh} compared with the experimental data, but in general they give larger local metal-cluster distortions. θ_m values are 1–2 degrees larger than experimentally reported in the molybdenum compounds, whereas the vanadium compounds show a similar but reversed trend in θ_m, i.e., 1–2 degrees smaller. This agreement is reasonable, and the difference in internal coordinates compared with experiment might come from low-resolution experimental characterization [10]. It is also possible that the structural phase transition is incomplete at low temperature [7]. We also find a minor trend that higher level functionals, as well as larger on-site Coulomb repulsion U values, favor larger structural distortions. Since our DFT simulations are performed at 0 K, while laboratory characterizations are performed at finite temperature, our results are more likely to capture the correct ground-state structure where thermal expansion effects are small.

It is interesting to note that the vanadium and molybdenum compounds show reversed structural distortions across the phase transition. This can be explained from the valence MO diagram in Fig. 2. In the cubic phase, there is either 1 electron (GaV_4S_8) or 5 electrons ($GaMo_4S_8$) in the valence t_2 orbitals. Such electronic configurations are Jahn-Teller active, whereby a structural distortion accompanied by orbital-degeneracy lifting could further stabilize the system. Owing to the different electron occupations in the vanadium and molybdenum compounds, their favored electronic configurations require a reversed ordering of the a_1 and e orbitals. Therefore, the spontaneous structural distortion permits each compound to lift its orbital degeneracy and achieve its favored electronic configuration.

We now summarize the structural benchmark assessment of the cubic and rhombohedral phases. We recommend using the GGA + U method for lattice structure relaxations with a Hubbard-U value of approximately 2 to 3 eV. The LDA functional should be used with on-site Coulomb interactions for both the cubic and rhombohedral phases. The SCAN functional is another reasonable choice that predicts accurate

lattice structures. Structural relaxations with HSE06 give very accurate lattice constants, but its high computational costs may be prohibitive if only trying to obtain reasonable crystal structures.

3. Magnetism

We find that the DFT ground state of both the molybdenum and vanadium compounds in the distorted $R3m$ structure are ferromagnetic with 1 μ_B/f.u. (Simulation of the complex magnetic phase diagram of lacunar spinels is out of the scope of this work; readers with interest should refer to Refs. [2,3,48–53].) In the molybdenum compounds, the magnetic moment is evenly distributed about all four Mo atoms, which is the same as what we found in the cubic phase. In the vanadium compounds, however, the apical V atom along the C_{3v} symmetry axis has a large local magnetic moment. The other three basal V atoms have relatively smaller moments that are antialigned to the apical spin. This results in a ferrimagnetic configuration in the V_4 cluster, giving a net-magnetic moment of 1 μ_B per formula unit. For instance, in the rhombohedral phase of GaV_4S_8 with the PBE functional, the magnetic moment on the apical V atom is 1.3 μ_B while the three basal V atoms contribute each −0.1 μ_B. Thus, the magnetization of GaV_4S_8 is 1 μ_B/f.u.. Some DFT functionals [e.g., PBE + U = 1.0 eV] are able to stabilize a ferromagnetic configuration in GaV_4S_8 similar to that of $GaMo_4S_8$, i.e., evenly distributed, but this magnetic configuration is less energetically favorable compared with the ferrimagnetic configuration. We report properties of the rhombohedral phase vanadium compounds using the ferrimagnetic configuration in the remainder of the paper. A recent work that used random-phase approximation correctly reproduced the ground state of GaV_4Se_8 and explored the coupling between magnetism and structure [54].

4. Electronic structures

We examine the electronic structures of rhombohedral GaV_4S_8, $GaMo_4S_8$, $GaNb_4Se_8$, and $GaTa_4Se_8$ in this section, because there is evidence that symmetry breaking in the transition-metal clusters without distortion of the lattice parameters could lead to different magnetic configurations [29]. Such small local distortions may also be challenging
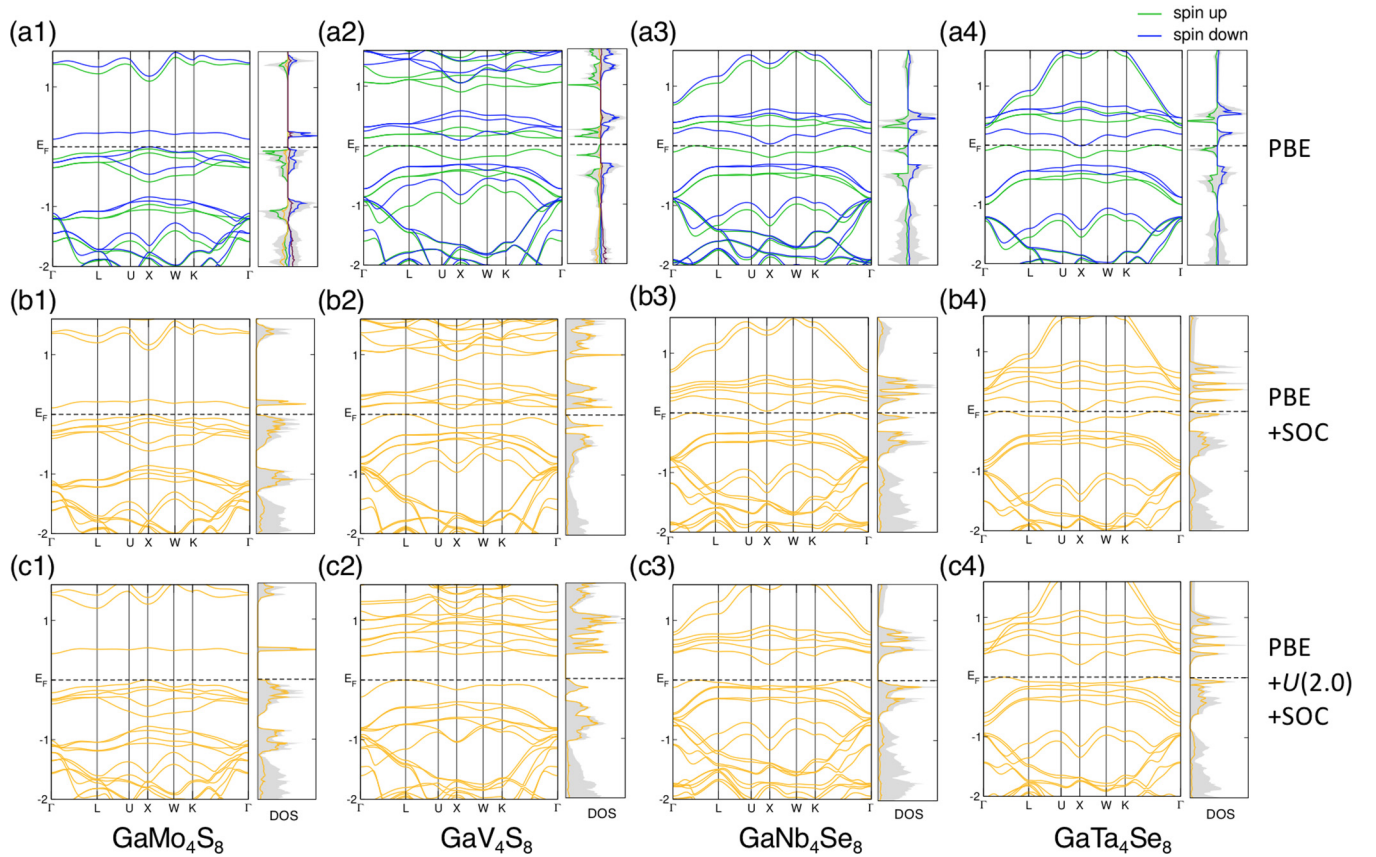
FIG. 9. DFT-PBE ground-state band structures and density of states (DOS) of the rhombohedral $R3m$ lacunar spinels. The second and third rows show simulation results with SOC. Color representation and the vertical energy axis are the same as that in Fig. 5.

to detect with low-resolution characterization techniques; for that reason, we hypothesize that the niobium- and tantalum-based lacunar spinels could also exhibit a distorted rhombohedral phase. Therefore, we slightly distort the cubic niobium and tantalum lacunar spinel structures along the symmetry-breaking pathway and use these geometries as the initial structure for structural relaxations. The structural relaxation settings using different DFT functionals are similar to those used for the cubic phase.

Figure 9(a)[1–4] presents the electronic band structures and projected DOSs of these four compounds. The triply degenerate valence bands in the cubic phase split into two sets of orbitals with a_1 and e symmetry. In the molybdenum compounds, the minority spin a_1 orbital shifts to higher energy, above the Fermi level, such that five valence electrons occupy the three majority spin orbitals and the minority e orbitals. The vanadium, niobium, and tantalum compounds exhibit different orbital occupations and structural distortions; the a_1 orbital is further stabilized to lower energy relative to the other five orbitals, and only one valence electron occupies the a_1 orbital. Remarkably, we find that the PBE functional is able to open up a small band gap without any on-site Coulomb interactions in the distorted phase of GaV_4S_8 and $GaMo_4S_8$. For $GaNb_4Se_8$ and $GaTa_4Se_8$, the lowest conduction band (minority a_1) barely touches the Fermi level. However, LDA predicts an unreasonable metallic ground state for these compounds. This finding indicates that the structural distortion alone is sufficient to lift the

orbital degeneracy and open a semiconducting gap without strong electron-correlation effect—apparently the additional electron density gradient in V_{xc} through the enhancement factor provides an improved description. In other words, the rhombohedral lacunar spinels may not be strictly described as "Mott" insulators. Our findings confirm the importance of local structural distortions on the electronic structures in lacunar spinels [10].

Meanwhile, different GGA functionals qualitatively describe the rhombohedral electronic structures differently. For instance, in GaV_4S_8, PBEsol predicts a metallic state, while PBE opens a small gap of 0.09 eV. In $GaMo_4S_8$, PBEsol gives a very small band gap of 0.02 eV while PBE predicts a band gap of 0.13 eV, which is much closer to the experimentally estimated value of 0.2 eV. Therefore, DFT-GGA simulations on this family of compounds should be performed with extra caution with attention focused on the role of the enhancement factor in reducing the self-interaction error [55]. We recommended that when using the PBEsol functional to simulate the electronic structures of the lacunar spinels, a slightly larger (≈ 1 eV) Hubbard U value is used than that for PBE.

Figure 9(b)[1–4] shows the electronic structures with the PBE functional and SOC. The effect of including SOC is similar to that in the cubic phase; orbital degeneracy is lifted, but the overall band structures remain similar. Figure 9(c) [1–4] shows the effect of now adding an on-site Coulomb interaction of 2.0 eV. All four compounds now exhibit a clear band gap, where the conduction band is
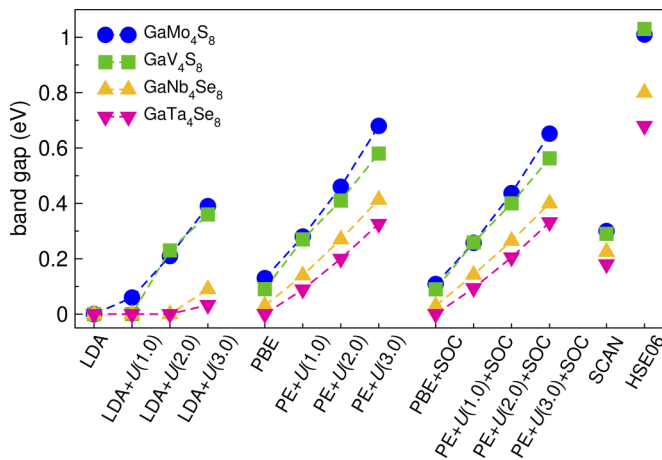
FIG. 10. DFT-functional dependence of the electronic band gaps for lacunar spinels in the rhombohedral $R3m$ structure.

pushed to higher energy owing to stronger electron-electron interactions. Interestingly, we find that SOC does not seem to play a decisive role in predicting reasonable electronic structures in the rhombohedral phase, whereas the GGA functional alone could predict qualitatively correct behavior. It is possible that SOC plays a less significant role here since crystal symmetry is already broken in the rhombohedral phase, unlike in the highly symmetric cubic phase. Our findings here support our previous hypothesis about the roles of SOC and electron-correlation in predicting semiconducting phases.

Figure 10 shows the different band gaps predicted using different DFT functionals. The decreasing band gap in the V-Nb-Ta series from $3d$ to $5d$ agrees well with our physical intuition, where electron-correlation effects are expected to decrease. The reason why molybdenum compounds show large band gaps might be caused by different orbital occupations—more valence electrons lead to larger orbital repulsion, which pushes the conduction band to a higher energy level, leading to a larger band gap. We also observe a higher functional rather than compositional dependency on the band gap. With an increasing on-site Coulomb repulsion U value, the band gap increases monotonically. Since a larger on-site Coulomb interaction effectively increases the repulsion between bands

with the same spin, it results in a larger gap between the highest occupied and lowest unoccupied bands.

We also observe an interesting similarity in Figs. 8 and 10, where the functional dependency of the Wyckoff position $3a$ (z_1) in GaV_4S_8 is similar to the trend in the band gap. A larger structural distortion in GaV_4S_8 also leads to a higher electronic band gap. $GaMo_4S_8$, however, does not exhibit such correlated features. The distinct behaviors of the Mo and V compounds indicate rather different relationships between the structural distortion and the ground-state electronic structures. Niobium and tantalum compounds have relatively smaller band gaps compared with vanadium and molybdenum ones, which is consistent with experimental estimations of the band gaps. It is also clear that including SOC has a negligible effect on ground-state band gap in all four compounds studied here.

SCAN predicts band gaps close to the experimentally suggested 0.2 ± 0.1 eV value [5], whereas HSE06 finds approximately a 1.0-eV band gap for the vanadium and molybdenum chalcogenides and around 0.7 eV for the niobium and tantalum compounds. Since the hybrid functionals partially correct the self-interaction problem in DFT, it is expected to predict more accurate band gaps than lower rung functionals. The larger portion of nonlocal and range-separated exact exchange interactions included in HSE06, however, might also destroy the balance within the transition-metal cluster, causing the large deviations in the band gaps of the lacunar spinels. It has also been reported that the ferromagnetic ground state is determined by the symmetric exchange interactions [29], which could possibly explain the different behaviors of HSE06 from lower level functionals. More careful experimental characterization of the distorted phase band gaps is required to have a better understanding of which V_{xc} performs the best.

We next examine the effect of the on-site Coulomb interactions and exact exchange interactions on the electronic structures of rhombohedral $GaMo_4Se_8$ (Fig. 11). The band structure and DOS of $GaMo_4Se_8$ using PBE functional with on-site Coulomb repulsion U values of 0.0, 1.0, 2.0, and 3.0 eV are shown in the first five panels. The four panels starting from the right of Fig. 11 correspond to the DOS obtained using the HSE06 functional with different portions of exact exchange included, as indicated in parentheses. In general, we observe very similar DOS for the occupied bands. The three valence bands in the spin-up channel are slightly
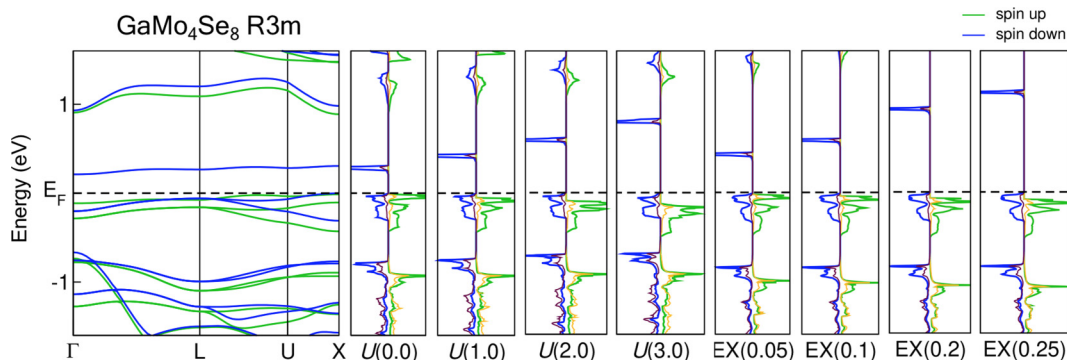

FIG. 11. Effect of on-site Coulomb interactions (U values of 0.0, 1.0, 2.0, and 3.0 eV) and the amount of exact exchange interactions in the hybrid HSE functional (EX values of 0.05, 0.1, 0.2, and 0.25) on the electronic structures of rhombohedral $R3m$ $GaMo_4Se_8$. EX = 0.25 corresponds to the standard amount of exact exchange in HSE06. The band structure panel on the left is obtained using the PBE functional.
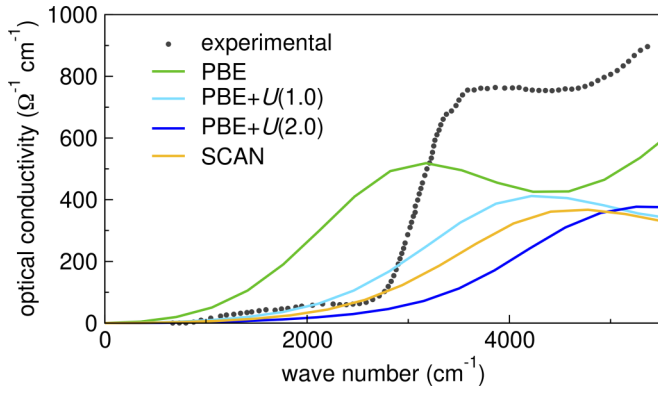
FIG. 12. DFT calculated optical conductivity of GaV_4S_8 in the rhombohedral $R3m$ structure compared with the experimental values obtained from Ref. [20].

FIG. 13. Phonon frequencies of GaV_4S_8 in the cubic (left panel) and rhombohedral (right panel) phase with different DFT functionals. The experimental data from Ref. [57] is reproduced in the first column labeled "Raman/IR."

shifted to lower energy relative to the Fermi level, E_F, with either larger U values or larger amounts of exact exchange. The orbitals beneath these valence orbitals, approximately located at -1 eV, are always lower in energy in our HSE06 calculations. Because the HSE06 functional treats all orbitals on the same footing, these lower energy orbitals are also "corrected" in a self-consistent manner, whereas the on-site Coulomb interaction through the $+U$ correction basically forces integer occupancy among only the correlated orbitals.

In addition, we find an increasing trend in the band gap with larger U values or greater contributions of exact exchange to V_{xc}. We find that $U = 1.0$–2.0 eV leads to very similar electronic structures obtained with HSE06 with 5–10% exact exchange. Our findings here suggest that a $GGA + U$ functional could be used as an alternative method to study electronic structures in lacunar spinels by reproducing the low-energy electronic structure obtained from a hybrid functional but at lower computational cost. The limitation is that lower lying orbitals that may be of interest are not corrected and therefore cannot exactly reproduce the results of the hybrid functional. Based on our simulation results, we do not suggest using the HSE06 functional for electronic structure simulations in the lacunar spinel family.

5. Optical conductivity

We compute the optical conductivity of the ferrimagnetic rhombohedral phase GaV_4S_8 and compare our DFT results with the experimental data [20] in Fig. 12. The experimental data shows the first optical transition occurs at ≈ 2700 cm^{-1} (black symbols), corresponding to an approximate 0.33-eV optical band gap. The optical conductivity then plateaus at approximately 800 Ω^{-1} cm^{-1} for higher frequencies. Our DFT simulations are able to semiqualitatively capture the plateau structure but do not quantitatively reproduce the optical conductivity. With increasing values of U, the plateau shifts to higher frequency and this behavior coincides with a larger optical gap as expected from the aforementioned band-gap dependencies on the exchange-correlation functional. The SCAN functional performs similar to PBE with $U = 1.0$–2.0 eV. PBE with $U = 2.0$ eV gives an optical gap closest to the experimental value. We note that because DFT is a single-particle ground-state theory, it may not be the
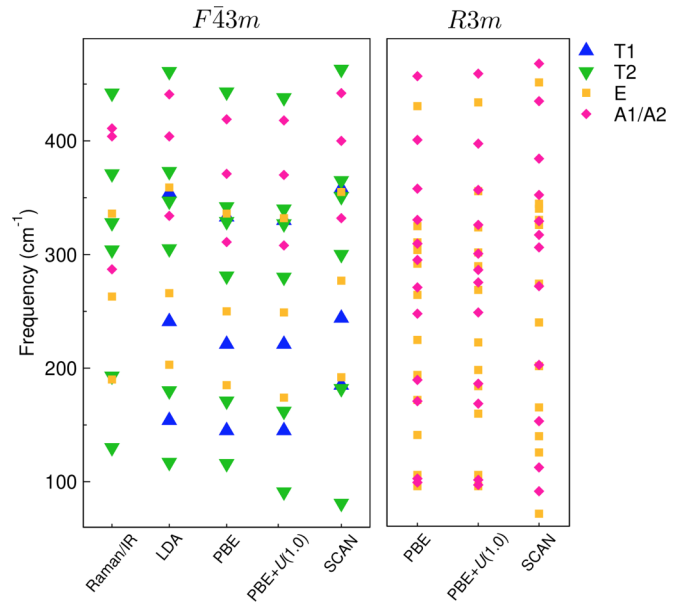
optimal tool to study excited-state properties, such as optical conductivity. More accurate simulations, for example, could be pursued by solving the Bethe-Salpeter equation using the GW quasiparticle energies [56].

6. Lattice dynamics

Last, we investigate the exchange-correlation functional dependency on the phonon frequencies in GaV_4S_8. We present our computed normal mode frequencies for both the cubic and rhombohedral phase with different functionals in Fig. 13: LDA, PBE, PBE $+ U = 1.0$ eV, and SCAN. These calculated values are compared with the experimental Raman/IR frequencies at 80 K reported in Ref. [57], which appear in the first column of Fig. 13. Note that the LDA results for the rhombohedral phase are not shown, because the $R3m$ structure is unstable at the LDA level.

We find that the cubic phase phonon frequencies generally agree well with experimental IR/Raman characterization data. LDA and PBE perform reasonably well in reproducing the phonon frequencies. However, with PBE $+ U = 1.0$ eV, we find a significant decrease in the frequency of the lowest T_2 phonon mode. The same behavior is also obtained with the SCAN functional. Interestingly, this T_2 mode mainly corresponds to the distortion of the transition-metal cluster along the symmetry-breaking pathway. This could be an evidence of electron-phonon-coupling–induced structure instability [13]. Although no Raman/IR data is available for the rhombohedral phase, we still see the same phonon mode softening with functional choice upon going from PBE to SCAN. The major difference between different functionals is at the low-frequency domain, where the vibrational modes are mainly related to the transition-metal (V_4) clusters. Our findings here suggest that lattice dynamics in the lacunar

spinels also have non-negligible functional dependency. More experimental (temperature-dependent) data, however, is required to ascertain the functional that best reproduces the lattice dynamical properties.

IV. CONCLUSIONS

In conclusion, LDA underperforms the other functionals and we recommended using it only with on-site Coulomb interactions added. The GGA functionals (PBE and PBEsol) perform reasonably well, and the results can be quantitatively improved with on-site Coulomb interactions explicitly added. The meta-GGA functional SCAN is another alternative choice that works well and does not require extra parametrization. Last, the hybrid functional HSE06 predicts accurate lattice structures but leads to a large electronic band gap in the low-temperature rhombohedral phase. Owing to its high computational cost as well as large deviation in electronic structure predictions, we do not recommend using this hybrid functional for the lacunar spinel family.

All exchange-correlation functionals predict reasonable lattice constants in both the cubic and rhombohedral polymorphs of the chalcogenide lacunar spinels. For electronic structure simulations, the cubic phase is always metallic from band theory and exhibits a narrow transition-metal-derived bandwidth at the Fermi level. Spin-orbit interactions are necessary to predict a semiconducting state in the cubic phase but not in the rhombohedral phase at the DFT level. At the LDA and GGA levels, on-site Coulomb interactions of 2 to 3 eV are recommended to obtain quantitatively improved results. We also found that the PBE functional without on-site Coulomb interactions could predict stable semiconducting states for the rhombohedral phase. Our results obtained with SCAN are similar to PBE $+ U = 2$ eV and thus can be safely used in simulations. We also find a highly spin-polarized DFT ground state in GaV_4S_8, which differs from available experimental data, motivating additional investigations of the magnetic order. We found that the single-particle DFT simulations of the optical conductivity do not give a quantitatively satisfying description of GaV_4S_8; more sophisticated methods such as with the *GW* method may be necessary to treat the excited state properties in the lacunar spinels. The LDA and PBE functionals, however, perform well in predicting the cubic phase phonon frequencies in GaV_4S_8.

[1] A. Camjayi, C. Acha, R. Weht, M. G. Rodríguez, B. Corraze, E. Janod, L. Cario, and M. J. Rozenberg, Phys. Rev. Lett. **113**, 086404 (2014).

[2] I. Kézsmárki, S. Bordács, P. Milde, E. Neuber, L. Eng, J. White, H. Rønnow, C. Dewhurst, M. Mochizuki, K. Yanai, H. Nakamura, D. Ehlers, V. Tsurkan, and A. Loidl, Nat. Mater. **14**, 1116 (2015).

[3] S. Widmann, E. Ruff, A. Günther, H.-A. Krug von Nidda, P. Lunkenheimer, V. Tsurkan, S. Bordács, I. Kézsmárki, and A. Loidl, Philos. Mag. **97**, 3428 (2017).

[4] R. Pocha, D. Johrendt, and R. Pöttgen, Chem. Mater. **12**, 2882 (2000).

[5] L. Cario, C. Vaju, B. Corraze, V. Guiot, and E. Janod, Adv. Mater. **22**, 5193 (2010).

[6] Y. Sahoo and A. Rastogi, J. Phys. Condens. Matter **5**, 5953 (1993).

[7] M. Francois, W. Lengauer, K. Yvon, M. Sergent, M. Potel, P. Gougeon, and H. B. Yaich-Aerrache, Z. Kristallogr.-Cryst. Mater. **196**, 111 (1991).

[8] M. François, O. Alexandrov, K. Yvon, H. B. Yaich-Aerrache, P. Gougeon, M. Potel, and M. Sergent, Z. Kristallogr.-Cryst. Mater. **200**, 47 (1992).

[9] M. M. Abd-Elmeguid, B. Ni, D. I. Khomskii, R. Pocha, D. Johrendt, X. Wang, and K. Syassen, Phys. Rev. Lett. **93**, 126403 (2004).

[10] M. Sieberer, S. Turnovszky, J. Redinger, and P. Mohn, Phys. Rev. B **76**, 214106 (2007).

[11] B. Corraze, E. Janod, L. Cario, P. Moreau, L. Lajaunie, P. Stoliar, V. Guiot, V. Dubost, J. Tranchant, S. Salmon, M.-P.

Besland, V. T. Phuoc, T. Cren, D. Roditchev, N. Stéphant, D. Troadec, and M. Rozenberg, Eur. Phys. J. Special Topics **222**, 1046 (2013).

[12] A. Le Beuze, H. Loirat, M. Zerrouki, and R. Lissillour, J. Solid State Chem. **120**, 80 (1995).

[13] A. Rastogi, R. Tournier, A. Berton, M. Potel, R. Chevrel, and M. Sergent, J. Low Temp. Phys. **55**, 551 (1984).

[14] A. Rastogi and E. Wohlfarth, Phys. Status Solidi B **142**, 569 (1987).

[15] A. V. Powell, A. McDowall, I. Szkoda, K. S. Knight, B. J. Kennedy, and T. Vogt, Chem. Mater. **19**, 5035 (2007).

[16] D. Bichler, Magnetismus und strukturelle Phasenumwandlungen von Verbindungen mit tetraedrischen Metallclustern, Ph.D. thesis, Ludwig Maximilian University of Munich, Munich, Germany, 2010.

[17] Y. Fujima, N. Abe, Y. Tokunaga, and T. Arima, Phys. Rev. B **95**, 180410(R) (2017).

[18] N. Shanthi and D. Sarma, J. Solid State Chem. **148**, 143 (1999).

[19] R. Pocha, D. Johrendt, B. Ni, and M. M. Abd-Elmeguid, J. Am. Chem. Soc. **127**, 8732 (2005).

[20] S. Reschke, F. Mayr, Z. Wang, P. Lunkenheimer, W. Li, D. Szaller, S. Bordács, I. Kézsmárki, V. Tsurkan, and A. Loidl, Phys. Rev. B **96**, 144302 (2017).

[21] J. P. Perdew, K. Burke, and M. Ernzerhof, Phys. Rev. Lett. **77**, 3865 (1996).

[22] G. I. Csonka, J. P. Perdew, A. Ruzsinszky, P. H. T. Philipsen, S. Lebègue, J. Paier, O. A. Vydrov, and J. G. Ángyán, Phys. Rev. B **79**, 155107 (2009).

[23] J. Sun, A. Ruzsinszky, and J. P. Perdew, Phys. Rev. Lett. **115**, 036402 (2015).

[24] J. Heyd, J. E. Peralta, G. E. Scuseria, and R. L. Martin, J. Chem. Phys. **123**, 174101 (2005).

[25] A. van de Walle and G. Ceder, Phys. Rev. B **59**, 14992 (1999).

[26] P. Haas, F. Tran, and P. Blaha, Phys. Rev. B **79**, 085104 (2009).

[27] J. Paier, M. Marsman, K. Hummer, G. Kresse, I. C. Gerber, and J. G. Ángyán, J. Chem. Phys. **124**, 154709 (2006).

[28] S. L. Dudarev, G. A. Botton, S. Y. Savrasov, C. J. Humphreys, and A. P. Sutton, Phys. Rev. B **57**, 1505 (1998).

[29] J. T. Zhang, J. L. Wang, X. Q. Yang, W. S. Xia, X. M. Lu, and J. S. Zhu, Phys. Rev. B **95**, 085136 (2017).

[30] H. Müller, W. Kockelmann, and D. Johrendt, Chem. Mater. **18**, 2174 (2006).

[31] J. Tirado-Rives and W. L. Jorgensen, J. Chem. theory Comput. **4**, 297 (2008).

[32] C. Di Valentin, G. Pacchioni, and A. Selloni, Phys. Rev. Lett. **97**, 166803 (2006).

[33] J. He and C. Franchini, Phys. Rev. B **86**, 235117 (2012).

[34] K. Hummer, J. Harl, and G. Kresse, Phys. Rev. B **80**, 115205 (2009).

[35] M. Ramzan, Y. Li, R. Chimata, and R. Ahuja, Comput. Mater. Sci. **71**, 19 (2013).

[36] G. Kresse and J. Furthmüller, Phys. Rev. B **54**, 11169 (1996).

[37] G. Kresse and D. Joubert, Phys. Rev. B **59**, 1758 (1999).

[38] P. E. Blöchl, Phys. Rev. B **50**, 17953 (1994).

[39] P. E. Blöchl, O. Jepsen, and O. K. Andersen, Phys. Rev. B **49**, 16223 (1994).

[40] A. Belsky, M. Hellenbrandt, V. L. Karen, and P. Luksch, Acta Crystallogr. Sect. B **58**, 364 (2002).

[41] Crystal structures available at our group GitHub page https://github.com/MTD-group/lacunar_spinel_structures.

[42] A. Togo and I. Tanaka, Scr. Mater. **108**, 1 (2015).

[43] J. Lynn, W. Ratcliff, M. Bleuel, L. Zhang, and S. Cheong, Bull. Am. Phys. Soc. **63**, B22.00010 (2018).

[44] H.-S. Kim, K. Haule, and D. Vanderbilt, arXiv:1810.09495 (unpublished).

[45] Z. Wang, E. Ruff, M. Schmidt, V. Tsurkan, I. Kézsmárki, P. Lunkenheimer, and A. Loidl, Phys. Rev. Lett. **115**, 207601 (2015).

[46] H.-S. Kim, J. Im, M. J. Han, and H. Jin, Nat. Commun. **5**, 3988 (2014).

[47] M. Y. Jeong, S. H. Chang, B. H. Kim, J.-H. Sim, A. Said, D. Casa, T. Gog, E. Janod, L. Cario, S. Yunoki, M. J. Han, and J. Kim, Nat. Commun. **8**, 782 (2017).

[48] K. J. A. Franke, B. M. Huddart, T. J. Hicken, F. Xiao, S. J. Blundell, F. L. Pratt, M. Crisanti, J. A. T. Barker, S. J. Clark, A. C. V. Štefančič, M. C. Hatnean, G. Balakrishnan, and T. Lancaster, Phys. Rev. B **98**, 054428 (2018).

[49] Á. Butykai, S. Bordács, I. Kézsmárki, V. Tsurkan, A. Loidl, J. Döring, E. Neuber, P. Milde, S. C. Kehr, and L. M. Eng, Sci. Rep. **7**, 44663 (2017).

[50] E. Ruff, S. Widmann, P. Lunkenheimer, V. Tsurkan, S. Bordács, I. Kézsmárki, and A. Loidl, Sci. Adv. **1**, e1500916 (2015).

[51] H.-M. Zhang, J. Chen, P. Barone, K. Yamauchi, S. Dong, and S. Picozzi, Phys. Rev. B **99**, 214427 (2019).

[52] D. Ehlers, I. Stasinopoulos, V. Tsurkan, H.-A. Krug von Nidda, T. Fehér, A. Leonov, I. Kézsmárki, D. Grundler, and A. Loidl, Phys. Rev. B **94**, 014406 (2016).

[53] A. O. Leonov and I. Kézsmárki, Phys. Rev. B **96**, 214413 (2017).

[54] E. C. Schueller, J. L. Zuo, J. D. Bocarsly, D. A. Kitchaev, S. D. Wilson, and R. Seshadri, Phys. Rev. B **100**, 045131 (2019).

[55] J. P. Perdew, S. Kurth, A. C. V. Zupan, and P. Blaha, Phys. Rev. Lett. **82**, 2544 (1999).

[56] P. Liu, B. Kim, X.-Q. Chen, D. D. Sarma, G. Kresse, and C. Franchini, Phys. Rev. Mat. **2**, 075003 (2018).

[57] J. Hlinka, F. Borodavka, I. Rafalovskyi, Z. Docekalova, J. Pokorny, I. Gregora, V. Tsurkan, H. Nakamura, F. Mayr, C. A. Kuntscher, A. Loidl, S. Bordács, D. Szaller, H.-J. Lee, J. H. Lee, and I. Kézsmárki, Phys. Rev. B **94**, 060104(R) (2016).